

Including monopoles to a fully desingularized boundary element method for acoustics

Qiang Sun^{1, a)} and Evert Klaseboer²

¹*Australian Research Council Centre of Excellence for Nanoscale Biophotonics,
School of Science, RMIT University, Melbourne, VIC 3001,
Australia*

²*Institute of High Performance Computing, 1 Fusionopolis Way, Singapore 138632,
Singapore*

The inclusion of domain (point) sources into a three dimensional boundary element method while solving the Helmholtz equation is described. The method is fully desingularized which allows for the use of higher order quadratic elements on the surfaces of the problem with ease. The effect of the monopole sources ends up on the right hand side of the resulting matrix system. Several carefully chosen examples are shown, such as sources near and within a concentric spherical core-shell scatterer as a verification case, a curved focusing surface and a multi-scale acoustic lens.

^{a)}qiang.sun@rmit.edu.au

I. INTRODUCTION

On 31 August 2021 it is exactly 200 years ago that Hermann von Helmholtz was born. The equation named after him, the Helmholtz equation, is used to describe various kinds of wave phenomena in the frequency domain, such as acoustic waves (Helmholtz, 1896), electromagnetic waves (Klaseboer *et al.*, 2017; Sun *et al.*, 2017) and light (Sun *et al.*, 2020a,b). Sound waves carry information and energy and are therefore of importance for numerous applications ranging from fundamental science (Emmanuelli *et al.*, 2021) to biophysics (Hawkins and Popper, 2018, 2020; Zhang, 2016), sensing (Rivet *et al.*, 2021), characterization (Legg and Bradley, 2016), engineering (Savioja and Svensson, 2015; Vorländer, 2013) and music (Gonzalez *et al.*, 2021; Mores, 2021). On the other hand, sound waves can cause problems, the most obvious example is annoying or even hazardous noise (Dümen and Şaher, 2020; Finneran, 2015; Michaud *et al.*, 2007; Stöber and Thomsen, 2021). Such a broad spectrum of acoustic phenomena makes acoustics a very active research area.

In the current work, we focus on (linear) sound waves in the frequency domain which means that we assume a $e^{-i\omega t}$ time dependency for all quantities, with ω the angular frequency and t time. Such wave phenomena can be described by this Helmholtz equation:

$$\nabla^2\phi + k^2\phi = 0, \quad (1)$$

where ϕ represents the (velocity) potential and k the wavenumber. The same equation is also valid for the pressure. Often, the effect of the presence of a volume source is important. For example in simulating traffic noise, airplane noise (Lugten *et al.*, 2018) or other

localized sources of sound (Sheng *et al.*, 2020). This will be done here in the context of a boundary element method (BEM) framework. Using BEM for acoustics is still an active area of research (Chernokozhin *et al.*, 2021). In a lot of instances, there is no need to model an acoustic source exactly, but it can be simplified as a point source, here an acoustic monopole. This must now be considered as an actual physical singularity in the domain, to be distinguished clearly from the “artificial” singularities caused by the mathematics, caused by the Green’s function on the surface becoming singular.

The advantage of the boundary element method over finite volume methods is that, for problems with infinite boundaries, the radiation conditions at infinity are automatically satisfied and no mesh is needed anywhere else than on the boundaries. As we will see, the boundary element method can resolve the point monopoles easily in the formulation, while domain methods (volume methods) need very careful mesh strategies to represent the area near the point source (Kalayeh *et al.*, 2015).

The outline of the paper is as follows: in Section II the mathematical implementation of the inclusion of a monopole into a fully desingularized boundary element framework is described. The constructed numerical framework is then validated in Section III for a multi-domain concentric core shell configuration with an analytical solution given in Appendix A. From a physics point of view, the interesting phenomena will be described with the variation of the dimensionless parameter ka , where k is the wavenumber (Eq. 1) and a is a typical dimension of the scattered object. Two examples on focused soundwaves are shown to demonstrate the robustness and effectiveness of our method based on two different physical phenomena: one example with reflection as demonstrated in Section IV and the other with

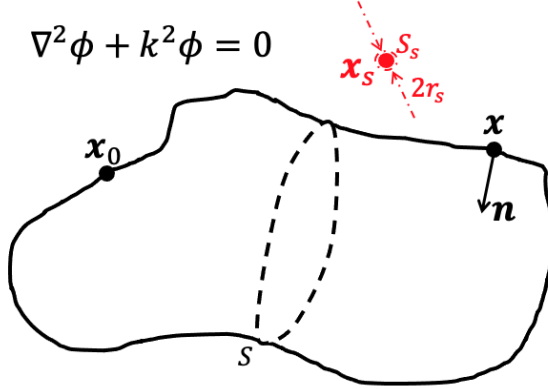


FIG. 1. Sketch of the parameters used in the boundary element method with a monopole (located at \mathbf{x}_s) included in the domain. The integrals must now be performed on the surface of the scatterer bounded by the surface S and on a small sphere with radius r_s around the monopole with surface S_s . In the theory the limit of $r_s \rightarrow 0$ is taken. A mathematical singularity arises in the conventional boundary element method when \mathbf{x} approaches \mathbf{x}_0 .

a multi-scale multi-domain acoustic lens as presented in Section V. Conclusions are given in Section VI.

II. INCLUSION OF A MONOPOLE IN A FULLY DESINGULARIZED BEM

The main goal of this work is to solve the Helmholtz equation, particularly in the presence of volume point sources, as sketched in Fig. 1. Since the Helmholtz equation is elliptic, in the standard boundary element framework the Helmholtz equation is rewritten as a surface integral on all surfaces S enclosing the computation domain in terms of the Green's function or kernel $G_k(\mathbf{x}, \mathbf{x}_0) \equiv e^{ik|\mathbf{x}-\mathbf{x}_0|}/|\mathbf{x}-\mathbf{x}_0|$ between the computation point \mathbf{x} and the observation point \mathbf{x}_0 as well as its normal derivative $H_k(\mathbf{x}, \mathbf{x}_0) = \mathbf{n} \cdot \nabla G_k(\mathbf{x}, \mathbf{x}_0)$ with \mathbf{n}

being the unit normal vector pointing out of the computational domain:

$$c(\mathbf{x}_0)\phi(\mathbf{x}_0) + \int_S \phi(\mathbf{x})H_k(\mathbf{x}, \mathbf{x}_0) - \frac{\partial\phi(\mathbf{x})}{\partial n}G_k(\mathbf{x}, \mathbf{x}_0)dS(\mathbf{x}) = -I_s. \quad (2)$$

In Eq. (2), the constant $c(\mathbf{x}_0)$ is the solid angle at \mathbf{x}_0 , and $\partial\phi(\mathbf{x})/\partial n \equiv \mathbf{n} \cdot \nabla\phi(\mathbf{x})$. As displayed in Fig. 1, we have drawn an artificial surface S_s around the monopole source and I_s is defined as: $I_s = \int_{S_s} [\phi_s H_k(\mathbf{x}, \mathbf{x}_0) - (\partial\phi_s/\partial n)G_k(\mathbf{x}, \mathbf{x}_0)]dS(\mathbf{x})$, with ϕ_s the potential near the monopole and \mathbf{x} is now located on S_s , while \mathbf{x}_0 is still situated on S . Thus the singular behavior of the integral I_s is now due to the singular behavior of ϕ instead of H_k and G_k . The term I_s will be determined later.

There are now two kinds of singularities in the problem. The first kind is of mathematical origin and is associated with the Green's function when the integration point \mathbf{x} approaches the point \mathbf{x}_0 on the surface S of the problem. The second (physical) singularity is due to the monopole in the domain. We will show that both singularities can be relatively easily dealt with in a fully non-singular boundary element framework.

Let us deal first with the mathematical singularity caused by the Green's function. There are several ways to desingularize this equation by subtracting a suitable similar solution that has the same singular behavior on the surface S , for example

$$c(\mathbf{x}_0)\psi(\mathbf{x}_0) + \int_S \psi(\mathbf{x})H_0(\mathbf{x}, \mathbf{x}_0) - \frac{\partial\psi(\mathbf{x})}{\partial n}G_0(\mathbf{x}, \mathbf{x}_0)dS(\mathbf{x}) = 0 \quad (3)$$

with $G_0(\mathbf{x}, \mathbf{x}_0) = 1/|\mathbf{x} - \mathbf{x}_0|$ and $H_0(\mathbf{x}, \mathbf{x}_0) = -(\mathbf{x} - \mathbf{x}_0) \cdot \mathbf{n}/|\mathbf{x}_s - \mathbf{x}_0|^3$ the Green's function for a Laplace problem and its normal derivative. Since Eq. (3) represents a Laplace equation, $\nabla^2\psi = 0$, a constant and a linear function are a solution. If ψ is chosen to be the following

combination of a constant and linear function

$$\psi(\mathbf{x}) = \phi(\mathbf{x}_0) + \mathbf{n}(\mathbf{x}_0) \cdot (\mathbf{x} - \mathbf{x}_0) \frac{\partial \phi(\mathbf{x}_0)}{\partial n}, \quad (4)$$

then the function ψ will approach $\phi(\mathbf{x}_0)$ when \mathbf{x} approaches \mathbf{x}_0 . Also, when the surface S is smooth then $\partial\psi(\mathbf{x}_0)/\partial n = \mathbf{n}(\mathbf{x}_0) \cdot \mathbf{n}(\mathbf{x}) \partial\phi(\mathbf{x}_0)/\partial n \rightarrow \partial\phi(\mathbf{x}_0)/\partial n$. When Eq. (3) is subtracted from Eq. (2), a totally non-singular boundary element framework emerges as:

$$\begin{aligned} & 4\pi\phi(\mathbf{x}_0) + \int_S [\phi(\mathbf{x})H_k(\mathbf{x}, \mathbf{x}_0) - \psi(\mathbf{x})H_0(\mathbf{x}, \mathbf{x}_0)] dS(\mathbf{x}) \\ &= \int_S \left[\frac{\partial\phi(\mathbf{x})}{\partial n} G_k(\mathbf{x}, \mathbf{x}_0) - \frac{\partial\psi(\mathbf{x})}{\partial n} G_0(\mathbf{x}, \mathbf{x}_0) \right] dS(\mathbf{x}) - I_s. \end{aligned} \quad (5)$$

The factor $4\pi\phi(\mathbf{x}_0)$ that appears in Eq. (5) originates from the fact that the integral at the surface at infinity can no longer be ignored for infinite domains, for instance the example demonstrated in Fig. 1. The term $\phi(\mathbf{x}_0)$ in Eq. (4) is responsible for this term. Note that the solid angle has disappeared from Eq. (5). Also, it is worth noticing that the singular behavior of G_k is in fact the same as G_0 since $G_k \equiv G_0 + \Delta G$ where $\Delta G \equiv (e^{ik|\mathbf{x}-\mathbf{x}_0|} - 1)/|\mathbf{x} - \mathbf{x}_0|$ is finite when $\mathbf{x} \rightarrow \mathbf{x}_0$, and the same analysis can be applied to H_k . The approach shown in Eq. (5) (but without the term I_s) was tested thoroughly in the past for Laplace problems and Stokes flow problems (Klaseboer *et al.*, 2012; Sun *et al.*, 2014, 2013, 2015a), Helmholtz equations (Sun *et al.*, 2015b), molecular and colloidal electrostatics (Sun *et al.*, 2016), and electromagnetic scattering theory using Helmholtz equations (Klaseboer *et al.*, 2017; Sun *et al.*, 2017). The desingularization using Eq. (3) is by no means the only way to desingularize the classical boundary element method, many alternative methods can be found (Klaseboer *et al.*, 2012; Sun *et al.*, 2015b). Since the desingularized boundary element method with high order elements, such as quadratic curved elements, is so accurate,

a further advantage is that it is very unlikely to hit an internal resonance frequency (and get a so-called spurious solution), thus there is no need to apply Burton-Miller type of schemes (Burton and Miller, 1971). For a more elaborate discussion on the fictitious frequency problem see (Klaseboer *et al.*, 2019). Also with the superior quadratic elements we only need a fraction of the nodes needed to get the same accuracy as with standard flat constant elements.

The next task is to determine the integral I_s over the surface S_s surrounding the small volume with the monopole source. The velocity potential of a monopole with constant complex strength Q is $\phi_s = Qe^{ikr_s}/(4\pi r_s)$, where Q represents the volume of fluid displaced by the source (Kinsler *et al.*, 2000), then $\partial\phi_s/\partial n = \mathbf{n} \cdot \nabla\phi_s = -Qd[e^{ikr_s}/(4\pi r_s)]/dr_s$. In the neighbourhood of S_s , this potential will totally overpower any other potentials and thus:

$$\begin{aligned} I_s &= \lim_{r_s \rightarrow 0} \int_{S_s} \left[\phi_s H_k(\mathbf{x}, \mathbf{x}_0) - \frac{\partial\phi_s}{\partial n} G_k(\mathbf{x}, \mathbf{x}_0) \right] dS(\mathbf{x}) \\ &\approx \lim_{r_s \rightarrow 0} \int_{S_s} Q \frac{e^{ikr_s}}{4\pi r_s} H_k(\mathbf{x}_s, \mathbf{x}_0) dS(\mathbf{x}) + \lim_{r_s \rightarrow 0} \int_{S_s} Q \frac{d}{dr_s} \left[\frac{e^{ikr_s}}{4\pi r_s} \right] G_k(\mathbf{x}_s, \mathbf{x}_0) dS(\mathbf{x}). \end{aligned} \quad (6)$$

Here we have used that $H_k(\mathbf{x}, \mathbf{x}_0)$ and $G_k(\mathbf{x}, \mathbf{x}_0)$ are not singular, since \mathbf{x} is situated on the surface S and \mathbf{x}_0 on S_s . For a very small sphere, $H(\mathbf{x}, \mathbf{x}_0)$ can thus be replaced by $H_k(\mathbf{x}_s, \mathbf{x}_0)$ and similar for G_k . The first integral with H_k behaves as $1/r_s \cdot r_s^2 \rightarrow 0$, since $dS \sim r_s^2$, and thus vanishes. The second integral becomes:

$$\lim_{r_s \rightarrow 0} \int_{S_s} Q \frac{d}{dr_s} \left[\frac{e^{ikr_s}}{4\pi r_s} \right] dS(\mathbf{x}) = \lim_{r_s \rightarrow 0} \int_{S_s} Q \frac{e^{ikr_s}}{4\pi r_s^2} (ikr_s - 1) dS(\mathbf{x}) = -Q \quad (7)$$

since $e^{ikr_s}(ikr_s - 1)/r_s^2 \sim -1/r_s^2$ and $dS = 4\pi r_s^2$. Thus:

$$I_s = \lim_{r_s \rightarrow 0} \int_{S_s} \left[\phi_s H_k(\mathbf{x}, \mathbf{x}_0) - \frac{\partial\phi_s}{\partial n} G_k(\mathbf{x}, \mathbf{x}_0) \right] dS(\mathbf{x}) = -Q \frac{e^{ik|\mathbf{x}_s - \mathbf{x}_0|}}{|\mathbf{x}_s - \mathbf{x}_0|}. \quad (8)$$

The above proof can easily be extended to multiple acoustic sources with different strengths placed at different locations in the domain. For example, for M monopoles one gets:

$$\begin{aligned} & 4\pi\phi(\mathbf{x}_0) + \int_S [\phi(\mathbf{x})H_k(\mathbf{x}, \mathbf{x}_0) - \psi(\mathbf{x})H_0(\mathbf{x}, \mathbf{x}_0)] dS(\mathbf{x}) \\ &= \int_S \left[\frac{\partial\phi(\mathbf{x})}{\partial n} G_k(\mathbf{x}, \mathbf{x}_0) - \frac{\partial\psi(\mathbf{x})}{\partial n} G_0(\mathbf{x}, \mathbf{x}_0) \right] dS(\mathbf{x}) + \sum_{i=1}^M Q_i \frac{e^{ik|\mathbf{x}_{s,i} - \mathbf{x}_0|}}{|\mathbf{x}_{s,i} - \mathbf{x}_0|}. \end{aligned} \quad (9)$$

Eq. (9) is the boundary regularised integral equation formulation including monopoles for acoustics used in this work. It is robust, efficient and accurate for solving multi-scale multi-domain acoustic problems. In particular, it is user-friendly and easy to be implemented together with high order elements since no treatment is needed to deal with singularities. To demonstrate this robustness, efficiency and accuracy, a few examples are presented in Sec. III to Sec. V. In all those simulations, 6-noded quadratic triangular elements ([Sun et al., 2016](#)) are used to represent the surfaces.

Note that the above described method (including the desingularization) can directly be applied to problems involving the Laplace equation ($k = 0$) as well. Now that ϕ and $\partial\phi/\partial n$ are known on the surface, through postprocessing the values of ϕ anywhere in the domain can be obtained. This can also be done in a desingularized manner, for more details see ([Sun et al., 2015b](#)).

In our soundwave simulations, we use three different kinds of boundary conditions. In the ‘solid surface’ scattering, it is assumed that the normal velocity on the surface of the scatterer is zero ($\partial\phi/\partial n = 0$). For simulations with two or more acoustic media, the boundary conditions across an interface are the continuity of the normal velocity (thus $\partial\phi/\partial n$ must be continuous across the interface) and the pressure (which assumes that $\rho\phi$ is continuous across the interface, with ρ the density), originating from the relationship $p = i\omega\rho\phi$ (with ω

the angular frequency of the system, see (Kirkup, 2007). Finally, for a bubble, it is assumed that the pressure at the bubble surface is zero, and thus $\phi = 0$.

III. VALIDATION WITH A CORE SHELL MODEL

To validate our non-singular boundary element method with domain monopoles included, we consider a concentric spherical core-shell scatterer in an external medium as shown in Fig. 2(a). There is one monopole in the scatterer core, Q^{core} one in the scatterer shell, Q^{shell} and one in the surrounding medium (the external domain), Q^{ex} to drive the acoustic field simultaneously. These three monopoles are located along the axis of symmetry of the spheres, the z axis of the Cartesian coordinate system with its origin locating at the centre of the core-shell spherical scatterer. In Appendix A, the analytical solution of such a problem is obtained.

The physical and geometrical parameters are: for the radii ratio, $a_{\text{shell}}/a_{\text{core}} = 2$; with the wavenumber for the external domain k_0 satisfying $k_0 a_{\text{core}} = 1$, the ratio of wavenumbers of the inner and shell are $k_1/k_0 = 1.5$ and $k_2/k_0 = 0.8 + i0.6$, respectively. Note, that k_2 has been chosen to be complex (i.e it will caused damping). The source strengths are chosen to be (note that we have deliberately chosen two of them out of phase and one with an imaginary number to validate our method) $Q^{\text{ex}} = 0.8 + i0.6$ at $r_s^{\text{ex}}/a_{\text{core}} = 3$, $Q^{\text{shell}} = 1.0$ at $r_s^{\text{shell}}/a_{\text{core}} = 1.5$, $Q^{\text{core}} = -1.0$ at $r_s^{\text{core}}/a_{\text{core}} = 0.5$. Finally the density ratios of the core and shell with respect to the outer medium are $\rho_1/\rho_0 = 5$ and $\rho_2/\rho_0 = 2$, respectively. The comparison with the theory has been done on three circular tracks, centered at the origin, one in the external domain, one in the shell and one in the core, all in the xz plane,

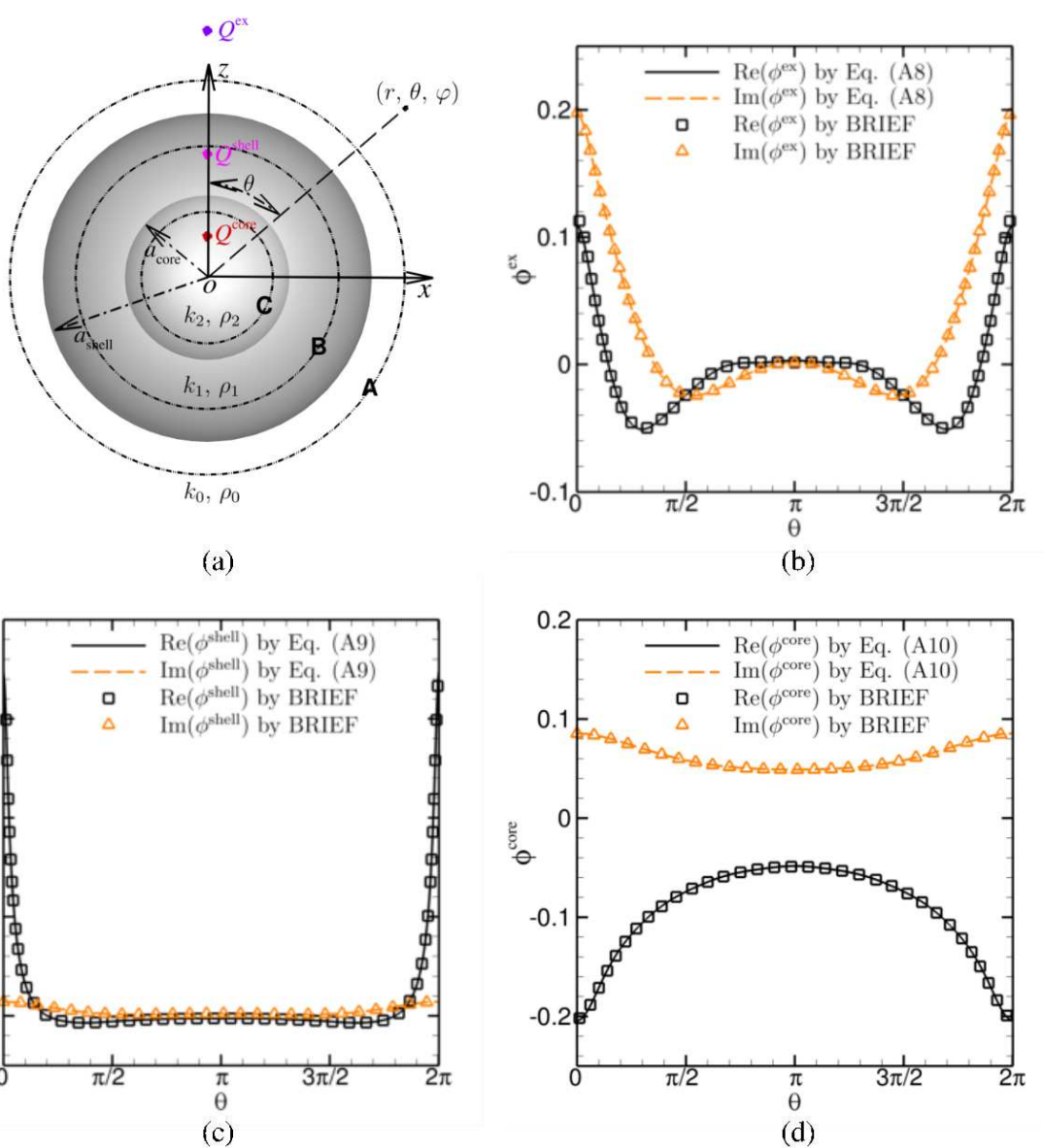


FIG. 2. Excellent agreement is shown between the analytical results obtained from Eqs. (A8) to (A10) and the numerical results obtained by using the boundary element method for the potential in the external domain (b), in the shell (c) and in the core (d) when a concentric spherical core-shelled scatterer is excited by three acoustic monopoles. The analytical results are indicated by lines and the numerical results by symbols.

as displayed in Fig. 2 (a) with dashed lines, indicated with **A**, **B** and **C**. The radii of the these three tracks are $r_{\mathbf{A}}/a_{\text{core}} = 2.4$, $r_{\mathbf{B}}/a_{\text{core}} = 1.6$ and $r_{\mathbf{C}}/a_{\text{core}} = 0.8$. For the case with the parameters mentioned above, the number of terms of the sum in Eqs. (A8) to (A10) is calculated to be $N = 6$. The values of each of the wavenumbers k are specially selected to make sure that N for each monopole is comparable. As shown in Fig. 2(b)-(d), excellent agreement is obtained between the analytical results from Eqs. (A8) to (A10) and the numerical results when 642 nodes connected by 320 quadratic elements are used for the shell and the same number for the core surface. The numerical and theoretical solutions are virtually overlapping.

The numerical implementation of this multi-domain (3-domain) boundary element problem consists of a few steps. First, we discretise the two surfaces, say N_{shell} nodes on the interface between the shell and the external domain and N_{core} on the surface in between the shell and the core particle. For the external domain we then get N_{shell} equations from Eq. 5, one for each node \mathbf{x}_0 . It appears most convenient to express all variables in terms of the shell potential. With the boundary conditions we thus get $\phi^{\text{ex}} = \phi^{\text{shell}} \rho_1 / \rho_0$ and $\partial \phi^{\text{ex}} / \partial n = \partial \phi^{\text{shell}} / \partial n$. For the shell domain a similar boundary element method will be applied for each node on the surfaces that enclose the computation domain which are the shell surface and the core surface, as such now $N_{\text{shell}} + N_{\text{core}}$ in total. Also, k_0 is now replaced by k_1 , the term with 4π is no longer present since it is an internal domain, and the source term must be replaced. Finally, for the internal domain another N_{core} equations will be obtained with wavenumber k_2 . This will result in a matrix system of size $2(N_{\text{shell}} + N_{\text{core}}) \times 2(N_{\text{shell}} + N_{\text{core}})$

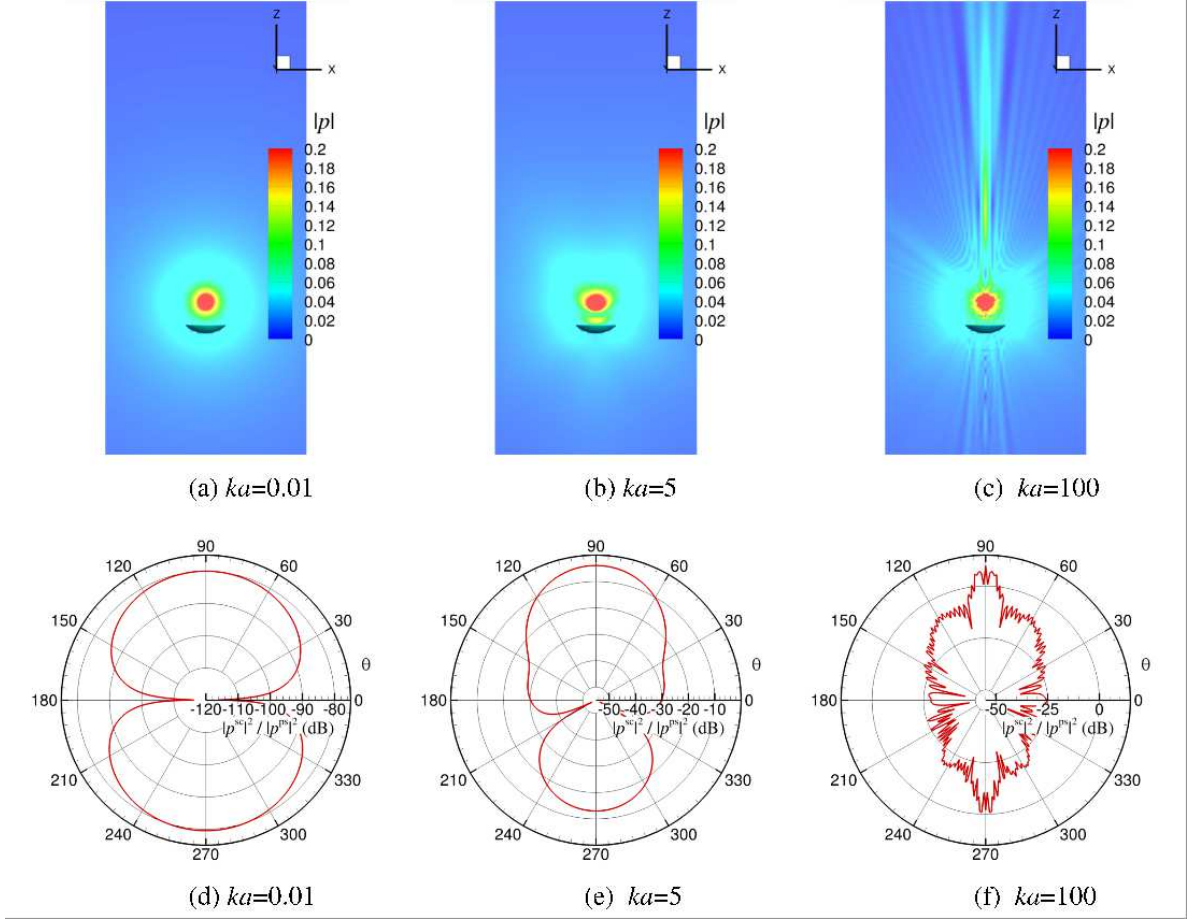


FIG. 3. Simulation of a bowl shaped object with a monopole placed at the focal point of the bowl.

The horizontal scale of the bowl is $2a$. For $ka = 0.01$, the wave essentially does not ‘see’ the bowl and the radar plot is (d) essentially becomes that of a dipole. For $ka = 5$ (b) and (e) a marked reflection can be observed. For $ka = 100$, (c) and (f) a very strong upward reflecting beam can be observed. In (a)-(c), the pressure is normalized by the pressure of the monopole at $r = |Q\rho_0\omega|/(4\pi)$ in the external domain. The radar plots (d), (e) and (f) were taken at $r = 100a$.

which can now be solved to get the unknowns ϕ^{shell} and its normal derivative $\partial\phi^{\text{shell}}/\partial n$ on both the shell surface and core surface.

IV. ONE OR MORE MONOPOLES NEAR A BOWL SHAPED OBJECT

Now that it is clear that the constructed numerical framework is reliable and accurate, we will show some further examples of interesting situations with a monopole interacting with a scatterer for which no analytical solutions are available.

As shown in Fig. 3(a)-(c), we consider a monopole source placed next to the concave surface of a rigid bowl shaped object in a medium with density of ρ_0 and the scattering from this object is simulated. From a physics point of view, it is interesting to investigate the effect of the wavelength on the scattered pattern with respect to the size of the object (thus changing the variable ka). The bowl shape is given by $(x, y, z) = (a \sin \theta \cos \varphi, a \sin \theta \sin \varphi, 0.1a(\cos \theta - 1) + 0.3 \sin^2 \theta)$ with θ the polar angle and φ the azimuthal angle. The monopole is located along the axis of symmetry of the bowl at $(0, 0, 1.35a)$. At the surface of the rigid bowl, the normal velocity of the fluid is zero. The non-singular boundary element method including one monopole was used to calculate the pressure distribution in the surrounding area of the bowl and the far field scattered pattern when the wavelength of the acoustic wave generated by the monopole is much larger than, in the same order of, and much smaller than the size of the bowl. In these calculations, the bowl surface is represented by 2880 quadratic triangular elements connected by 5762 nodes. When the acoustic wavelength, λ with $k\lambda = 2\pi$, from the monopole is much larger than the size of the bowl as $ka = 0.01$, the acoustic wave is barely affected by the scatterer bowl. As such, the distribution of pressure, p , in the area surrounding the bowl is very similar to that of a single monopole in the free space (external domain), as shown in

Fig. 3(a), and at the far field, the scattered field, p^{sc} , is a dipole field as shown in Fig. 3(d). Here, p^{sc} is calculated by $p = p^{\text{sc}} + p^{\text{ps}}$ with p^{ps} the pressure of the monopole in the free space. When the wavelength of the acoustic field generated by the monopole is in the same order of the size of the bowl as $ka = 5$, the effect of the bowl on the acoustic field becomes obvious as the field is reflected and the field in front of the bowl is elongated as shown in both Figs. 3(b) and 3(e). When the wavelength is much smaller relative to the bowl size as $ka = 100$, ray phenomena are dominant. Since the monopole is located at the focal point of the concave bowl, a focused beam along the axis of symmetry appears, and the reflected acoustic field from the bowl is much stronger relative to the diffraction field at the back of the bowl, as shown in Figs. 3(c) and 3(f).

When the acoustic monopole is away from the symmetric axis of the blow with $ka = 100$, the reflection patterns were affected accordingly, as shown in Fig 4. When the monopole location is shifted horizontally to $(x_s, y_s, z_s) = (0.33a, 0, 1.35a)$, the reflected focused beam is rotated counterclockwise around the focal point of the concave bowl by about 13.75° (Fig. 4a). When the monopole is moved further away from the symmetric axis of the bowl to $(x_s, y_s, z_s) = (0.67a, 0, 1.35a)$, the focused beam rotates more in the counterclockwise direction (Fig. 4b). If the monopole is moved to the edge of the bowl at $(x_s, y_s, z_s) = (1.0a, 0, 1.35a)$, the focused beam almost vanishes (Fig. 4c).

A dipole can be constructed by two monopoles with opposite strength (fully out of phase) located very close to each other (here at a distance $10^{-5}a$). If this dipole is located at the focal point of the concave bowl, the acoustic pressure patterns are shown in Fig. 5. Since acoustic waves are longitudinal, when the dipole axis is aligned with the symmetry axis of

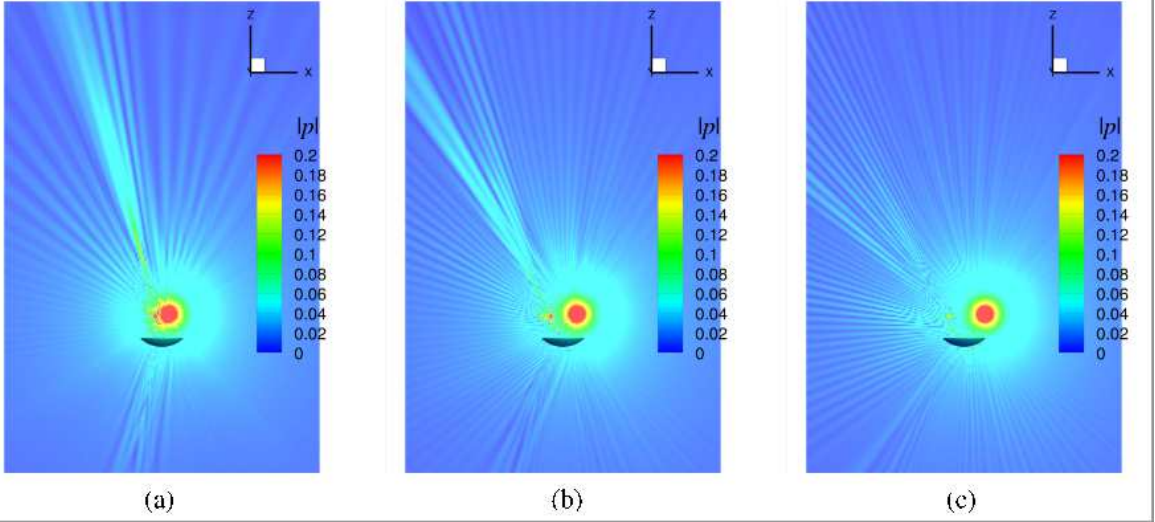


FIG. 4. The effect of changing the location of the monopole with respect to the bowl shaped object.

The monopole is placed $0.33a$ (a), $0.67a$ (b) and $1.0a$ (c) in the x-direction instead of on the axis of symmetry. the pressure is normalized by the pressure of the monopole at $r = |Q\rho_0\omega|/(4\pi)$ in the external domain.

the bowl, a strong focussed beam is formed from the reflected field of the bowl along its symmetric axis and the field is fully symmetric with respect to the bowl symmetry axis, as shown in Fig. 5(a). When the dipole axis is rotated $\pi/4$ clockwise with respect to the z -axis, the symmetry of the acoustic field is broken, as shown in Fig. 5(b). If the dipole axis is perpendicular to the symmetric axis of the rigid bowl, the symmetry of the field with respect to that axis is recovered with a low pressure field along that axis and two relative high pressure fields next to the axis due to the focus effect from the reflection field of the concave surface of the rigid bowl, as shown in Fig. 5(c).

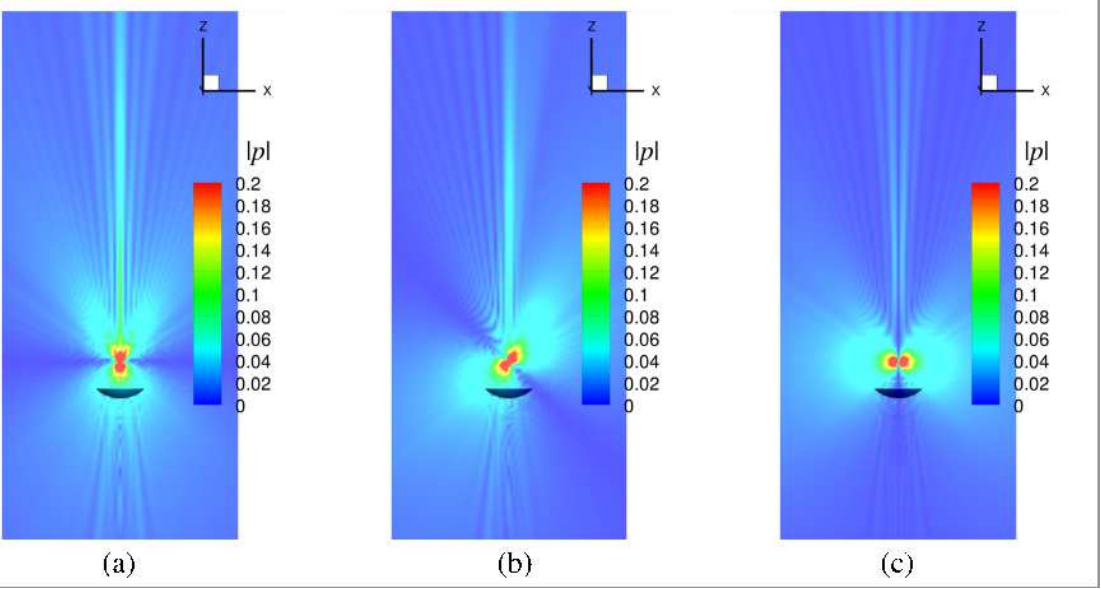


FIG. 5. Dipole at the focal point of the bowl shaped object. (a) dipole aligned with z -axis, (b) at a 45 degrees angle and (c) at a 90 degrees angle. In all three cases $ka = 100$. the pressure is normalized by the pressure of the dipole at $r = |Q\rho_0\omega|/(4\pi)$ in the external domain.

V. MULTI-SCALE MULTI-DOMAIN ACOUSTIC LENS

The next interesting example is an acoustic lens, comprising of a spherical oil drop of radius $a_{\text{drop}} = 2.39$ mm submerged in water, with or without a tiny rigid sphere or bubble included. The ensemble is being irradiated by five acoustic monopoles with frequency 1 MHz. The monopoles are aligned perpendicular to the drop as indicated in Fig.6(b) by the red dots. They are placed $h^{\text{ps}} = 1.19$ mm apart. The distance between the line of monopoles and the center of the oil drop is 8.4 mm (or $3.5a_{\text{drop}}$). The reference pressure amplitude obtained without the presence of the oil drop is shown in Fig.6(a). Next, the oil droplet is placed at the origin of the coordinate system in Fig.6(b). The presence of this oil droplet clearly creates a focal point at the back of the droplet ($\max |p| = 0.322$ at $x = 0.980a_{\text{drop}}$). The

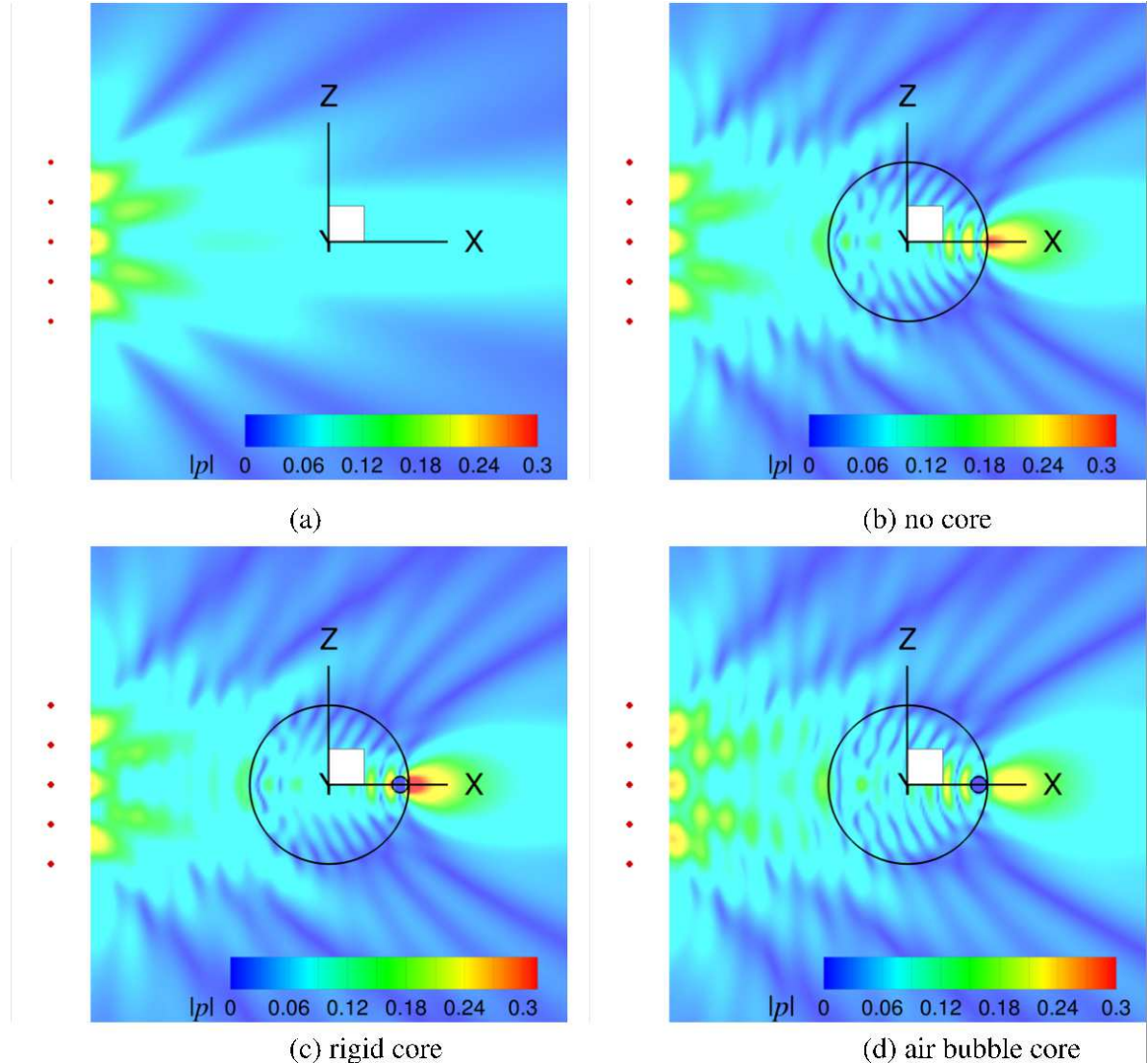


FIG. 6. Pressure amplitudes for 5 monopoles in water with (a) no drop, (b) an oil drop, (c) an oil drop with a tiny rigid sphere at the back and (d) an oil drop with a tiny air bubble at the back. The parameter are: $k_0a = 10$, $\rho_{\text{drop}}/\rho_0 = 0.8$, $k_{\text{drop}}/k_0 = 1.333$. The five monopoles are located at $x = -3.5a_{\text{drop}}$, $y = 0$, and $z = -a_{\text{drop}}$, $-0.5a_{\text{drop}}$, 0 , $0.5a_{\text{drop}}$ and a_{drop} , respectively (indicated with red dots). Maxima and minima at about half the wavelength appear due to interference of scattered and incoming waves appear in (b), (c) and (d), while a more or less uniform amplitude is observed in the area around $x=0$ in (a).

wavenumber in the external domain (water) is noted as k_0 with $k_0 a_{\text{drop}} = 10$ when the speed of sound in water is 1500 m/s. The density ratio of the oil drop to water is $\rho_{\text{drop}}/\rho_0 = 0.8$ and the ratio of the wavenumber is $k_{\text{drop}}/k_0 = 1.33$. The effects of surface tension have been ignored in the simulations. Both the surfaces of the oil drop and the small defect inside it are represented by 720 quadratic triangular elements connected by 1442 nodes. The pressure is normalized by the pressure of a single monopole at $r = |Q\rho_0\omega|/(4\pi)$ in the external domain.

It is instructive to investigate if this acoustic ‘lens’ can be affected by the presence of some defect inside the oil drop, a multi-scale multi-domain acoustic lens. For example the inclusion of a tiny particle at the back of the oil droplet changes noticeably the scattering pattern as clearly illustrated in Fig. 6(c), the focusing effect is stronger ($\max |p| = 0.398$ at $x = 0.980a_{\text{drop}}$) when compared to that of Fig. 6(b). Here, a rigid particle with radius $a_{\text{core}}/a_{\text{drop}} = 0.1$ is added with the minimum gap between the inner core and the oil shell $h_{\text{gap}}/a_{\text{drop}} = 0.01$. If an air bubble with the same size of that tiny particle is placed at the same location, the focal point is moved further away from the drop as presented in Fig. 6(d) and its amplitude is clearly decreased ($\max |p| = 0.244$ at $x = 1.221a_{\text{drop}}$). Thus an object smaller than the wavelength of sound can still have an observable influence on the formation of a focal point.

Snapshots of the time-harmonic pressure distributions are shown in Fig. 7 for both the oil drop with the rigid sphere and with the bubble. It is clear that the combined wave field of the five sources combined to a pseudo plane wave according to the Huygens principle before it hits the oil drop. The full animations are available as supplementary material.

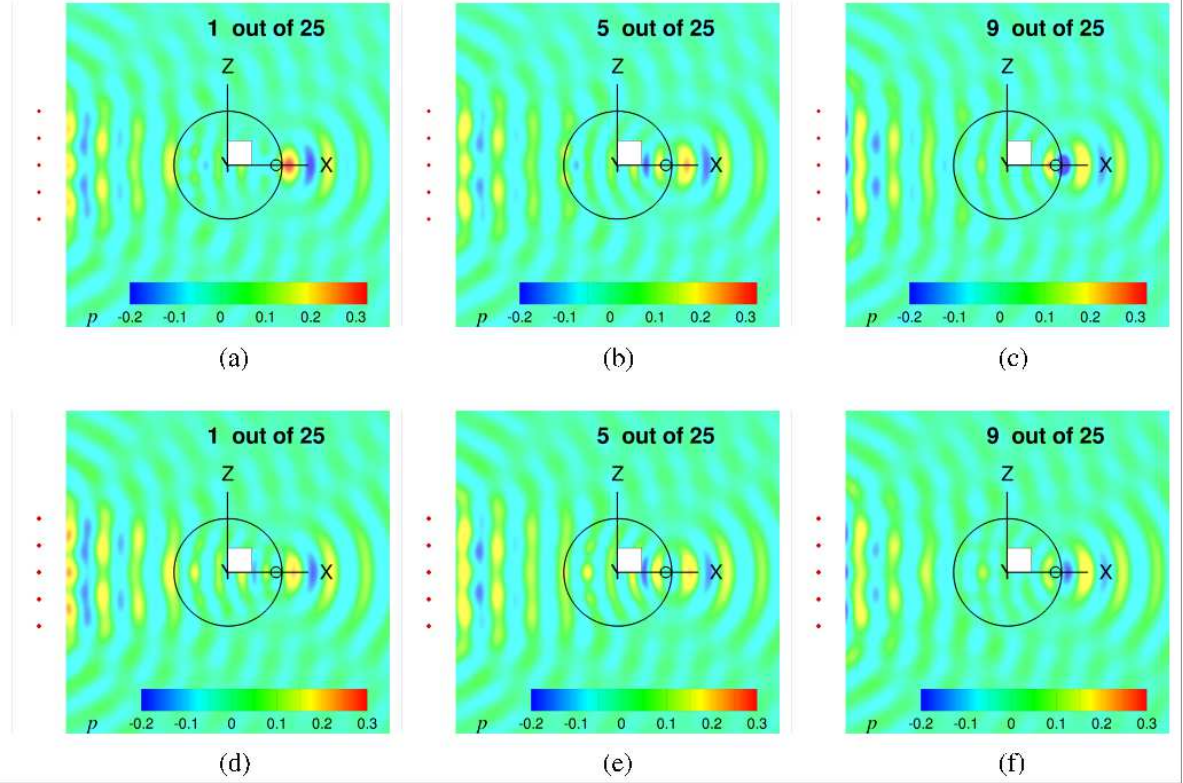


FIG. 7. As Fig.6, but instantaneous pressure profile at selected times: (a)-(c), rigid core; (d)-(f)

bubble core. The pressure is normalized by the pressure of a single monopole at $r = |Q\rho_0\omega|/(4\pi)$ in the external domain. Note the recombining spherical waves from the monopoles (the red dots) into a plane wave region in front of the drop. The interplay between reflected and transmitted waves results in a focal point just behind the drop. Full animations are available as supplementary material.

VI. CONCLUSIONS

A monopole representing a volume source can be relatively straightforward included in a boundary element framework for the Helmholtz equation. Several examples with focusing sound beams have been shown and a validation case based on a core shell sphere model for

which an analytical solution is available. In the boundary element framework shown here, the integrals are fully regular, resulting in a much better accuracy and efficiency since it allows the easy use of higher order elements to approximate curved scattering surfaces, and ensures robustness and effectiveness for solving multi-scale multi-domain acoustic problems.

ACKNOWLEDGMENTS

Q.S. would like to thank the support of an Australian Research Council Discovery Early Career Researcher Award (Grant No. DE150100169).

APPENDIX A: CORE-SHELL SCATTERER WITH MONOPOLES; THEORY

In this appendix, the analytical solution of the field driven by the acoustic monopoles located along the axis of symmetry of a concentric core-shell spherical scatterer is derived. As shown in Fig. 8, the centre of a core-shell spherical scatterer is set at the origin of a Cartesian coordinate system. The axis of symmetry of this spherical scatterer is chosen along the z -axis where the acoustic monopoles are also situated. To solve the acoustic field of such a system, it is most convenient to employ a spherical coordinate system which origin is at the center of the spherical scatterer and polar angle is measured from the z -axis.

Suppose that an acoustic point source (monopole) is situated at $\mathbf{x}_s \equiv (0, 0, r_s)$, (with $r_s = |\mathbf{x}_s|$). The expression of the acoustic field at $\mathbf{x} \equiv (r, \theta, \varphi)$, $\phi^{\text{ps}}(\mathbf{x}) \equiv \phi^{\text{ps}}(r, \theta)$, generated by such a monopole does not depend on the azimuthal angle φ and can be represented

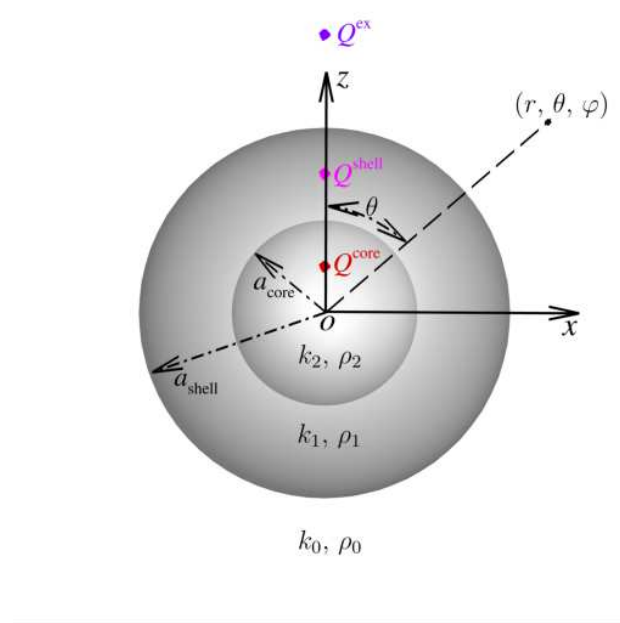


FIG. 8. Sketch of the physical problem when a concentric spherical core-shell scatterer is irradiated by three acoustic monopoles all located along the z -axis (the axis of symmetry). A Cartesian coordinate system and the companion spherical coordinate system are set with their origin at the centre of the spherical core.

asymptotically in terms of free spherical multipolar waves (Burke and Joachain, 1995) as

$$\begin{aligned}\phi^{\text{ps}}(\mathbf{x}) \equiv \phi^{\text{ps}}(r, \theta) &= \frac{Q}{4\pi} \frac{\exp(i k |\mathbf{x} - \mathbf{x}_s|)}{|\mathbf{x} - \mathbf{x}_s|} \\ &= \frac{Q}{4\pi} i k \sum_{n=0}^N (2n+1) h_n(kr_>) j_n(kr_<) P_n(\cos \theta)\end{aligned}\quad (\text{A1})$$

where Q is the strength of the acoustic monopole, \mathbf{x} is the position vector, $r_> \equiv \max(r, r_s)$, $r_< \equiv \min(r, r_s)$, k is the domain wavenumber, $h_n(kr_>)$ is the spherical Hankel function of the first kind, $j_n(kr_<)$ is the spherical Bessel function of the first kind, and N is number of terms in the sum (determining the truncated error). Inspired by Mie scattering theory, see (Bohren and Huffman, 1998), we propose that N can be estimated using the following

formula to balance the computational efficiency and stability with the truncated error (lower than 10^{-3}):

$$\begin{aligned} N &= |k| + 4|k|^{\frac{1}{3}} + 1 && \text{if } |\mathbf{x}_s| \geq \frac{1}{2}; \\ N &= |(k|\mathbf{x}_s|)| + 4|(k|\mathbf{x}_s|)|^{\frac{1}{3}} + 1 && \text{if } |\mathbf{x}_s| < \frac{1}{2} \end{aligned} \quad (\text{A2})$$

in which the expression on the right hand side is rounded off to the nearest integer.

Also, consider a scalar wave equation for function ϕ with wavenumber k :

$$\nabla^2 \phi + k^2 \phi = 0. \quad (\text{A3})$$

Eq. (A3) is variable separable in spherical coordinates, and its elementary solutions are in the form

$$\phi_{(l,n)} = \cos(l\varphi) P_n^l(\cos\theta) z_n(kr), \quad (\text{A4a})$$

$$\phi_{(l,n)} = \sin(l\varphi) P_n^l(\cos\theta) z_n(kr) \quad (\text{A4b})$$

where l and n are integers ($n \geq l \geq 0$), $P_n^l(\cos\theta)$ is an associated Legendre polynomial, and $z_n(kr)$ is the spherical Bessel function. The following rules are applied to determine the choice of the function $z_n(kr)$. In the bounded domain comprising the origin, $z_n(kr) \equiv j_n(kr)$, the spherical Bessel function of the first kind, is used since $j_n(kr)$ is finite at the origin. In the bounded domain excluding the origin, both $z_n(kr) \equiv j_n(kr)$ and $z_n(kr) \equiv y_n(kr)$, the spherical Bessel functions of the first and second kind, are needed. In the unbounded external domain, the spherical Hankel function $z_n(kr) \equiv h_n(kr) = j_n(kr) + iy_n(kr)$ is used since $ikh_n(kr) \sim i^n \exp(ikr)/r$, representing an outgoing wave. A good reference for all the special functions mentioned above can be found in NIST Digital Library of Mathematical

Functions (DLMF, 2020), and some useful recurrence relations in our derivation are listed below:

$$z_{n+1}(\zeta) = \frac{2n+1}{\zeta} z_n(\zeta) - z_{n-1}(\zeta) \quad n = 1, 2, \dots, \quad (\text{A5a})$$

$$\frac{dz_n(\zeta)}{d\zeta} \equiv z'_n(\zeta) = -z_{n+1}(\zeta) + \frac{n}{\zeta} z_n(\zeta) \quad n = 0, 1, \dots; \quad (\text{A5b})$$

$$j_0(\zeta) = \frac{\sin \zeta}{\zeta}, \quad (\text{A6a})$$

$$j_1(\zeta) = \frac{\sin \zeta}{\zeta^2} - \frac{\cos \zeta}{\zeta}, \quad (\text{A6b})$$

$$j_2(\zeta) = \left(-\frac{1}{\zeta} + \frac{3}{\zeta^3} \right) \sin \zeta - \frac{3}{\zeta^2} \cos \zeta, \quad (\text{A6c})$$

$$y_0(\zeta) = -\frac{\cos \zeta}{\zeta}, \quad (\text{A6d})$$

$$y_1(\zeta) = -\frac{\cos \zeta}{\zeta^2} - \frac{\sin \zeta}{\zeta}, \quad (\text{A6e})$$

$$y_2(\zeta) = \left(\frac{1}{\zeta} - \frac{3}{\zeta^3} \right) \cos \zeta - \frac{3}{\zeta^2} \sin \zeta; \quad (\text{A6f})$$

and

$$P_0(\cos \theta) = 1, \quad (\text{A7a})$$

$$P_1(\cos \theta) = \cos \theta, \quad (\text{A7b})$$

$$P_{n+2}(\cos \theta) = \frac{(2n+3) \cos \theta}{n+2} P_{n+1}(\cos \theta) - \frac{n+1}{n+2} P_n(\cos \theta). \quad (\text{A7c})$$

When comparing the expressions Eq. (A1) and Eq. (A4), and considering the discussion below Eq. (A1), we can write the acoustic fields, respectively, in the external domain when

$r \geq a_{\text{shell}}$ as

$$\begin{aligned}\phi^{\text{ex}}(r, \theta) = & \frac{Q^{\text{ex}}}{4\pi} ik_0 \sum_{n=0}^N (2n+1) h_n(k_0 r_>^{\text{ex}}) j_n(k_0 r_<^{\text{ex}}) P_n(\cos \theta) \\ & + \sum_{n=0}^N C_n h_n(k_0 r) P_n(\cos \theta),\end{aligned}\quad (\text{A8})$$

in the spherical shell when $a_{\text{core}} \leq r \leq a_{\text{shell}}$ as

$$\begin{aligned}\phi^{\text{shell}}(r, \theta) = & \frac{Q^{\text{shell}}}{4\pi} ik_1 \sum_{n=0}^N (2n+1) h_n(k_1 r_>^{\text{shell}}) j_n(k_1 r_<^{\text{shell}}) P_n(\cos \theta) \\ & + \sum_{n=0}^N [D_n j_n(k_1 r) + E_n y_n(k_1 r)] P_n(\cos \theta),\end{aligned}\quad (\text{A9})$$

and in the spherical core when $r \leq a_{\text{core}}$ as

$$\begin{aligned}\phi^{\text{core}}(r, \theta) = & \frac{Q^{\text{core}}}{4\pi} ik_2 \sum_{n=0}^N (2n+1) h_n(k_2 r_>^{\text{core}}) j_n(k_2 r_<^{\text{core}}) P_n(\cos \theta) \\ & + \sum_{n=0}^N F_n j_n(k_2 r) P_n(\cos \theta).\end{aligned}\quad (\text{A10})$$

In Eqs. (A10) to (A8), k_0 , k_1 and k_2 are the wavenumber in the external domain, the shell and the core, respectively; $r_>^{\text{ex}} \equiv \max(r, r_s^{\text{ex}})$, $r^< \equiv \min(r, r_s^{\text{ex}})$, $r_>^{\text{shell}} \equiv \max(r, r_s^{\text{shell}})$, $r^< \equiv \min(r, r_s^{\text{shell}})$, $r_>^{\text{core}} \equiv \max(r, r_s^{\text{core}})$, $r^< \equiv \min(r, r_s^{\text{core}})$, respectively; and C_n , D_n , E_n , F_n are the unknown coefficients to be determined by the boundary conditions.

To calculate the unknown coefficients in Eqs. (A8) to (A10), the boundary condition of the continuity of the acoustic pressure and that of the continuity of the radial velocity are used on the interface between the core and shell and that between the shell and external

domain (see also the discussion on boundary conditions in Section II). As such, we have

$$\rho_0 \phi^{\text{ex}}(a_{\text{shell}}, \theta) = \rho_1 \phi^{\text{shell}}(a_{\text{shell}}, \theta), \quad (\text{A11a})$$

$$\rho_1 \phi^{\text{shell}}(a_{\text{core}}, \theta) = \rho_2 \phi^{\text{core}}(a_{\text{core}}, \theta), \quad (\text{A11b})$$

$$\frac{\partial \phi^{\text{ex}}(r, \theta)}{\partial r} \bigg|_{r=a_{\text{shell}}} = \frac{\partial \phi^{\text{shell}}(r, \theta)}{\partial r} \bigg|_{r=a_{\text{shell}}}, \quad (\text{A11c})$$

$$\frac{\partial \phi^{\text{shell}}(r, \theta)}{\partial r} \bigg|_{r=a_{\text{core}}} = \frac{\partial \phi^{\text{core}}(r, \theta)}{\partial r} \bigg|_{r=a_{\text{core}}}. \quad (\text{A11d})$$

where ρ_0 , ρ_1 and ρ_2 are the density of the external domain, the shell and the core, respectively.

Introducing Eqs. (A8) to (A10) into Eq. (A11) leads to

$$\begin{aligned} & \rho_0 C_n h_n(k_0 a_{\text{shell}}) - \rho_1 [D_n j_n(k_1 a_{\text{shell}}) + E_n y_n(k_1 a_{\text{shell}})] \\ &= -\rho_0 \frac{Q^{\text{ex}}}{4\pi} i k_0 (2n+1) h_n(k_0 r_s^{\text{ex}}) j_n(k_0 a_{\text{shell}}) + \rho_1 \frac{Q^{\text{shell}}}{4\pi} i k_1 (2n+1) h_n(k_1 a_{\text{shell}}) j_n(k_1 r_s^{\text{shell}}) \end{aligned} \quad (\text{A12a})$$

$$\begin{aligned} & \rho_1 [D_n j_n(k_1 a_{\text{core}}) + E_n y_n(k_1 a_{\text{core}})] - \rho_2 F_n j_n(k_2 a_{\text{core}}) \\ &= -\rho_1 \frac{Q^{\text{shell}}}{4\pi} i k_1 (2n+1) h_n(k_1 r_s^{\text{shell}}) j_n(k_1 a_{\text{core}}) + \rho_2 \frac{Q^{\text{core}}}{4\pi} i k_2 (2n+1) h_n(k_2 a_{\text{core}}) j_n(k_2 r_s^{\text{core}}) \end{aligned} \quad (\text{A12b})$$

$$\begin{aligned} & C_n h'_n(k_0 a_{\text{shell}}) - [D_n j'_n(k_1 a_{\text{shell}}) + E_n y'_n(k_1 a_{\text{shell}})] \\ &= -\frac{Q^{\text{ex}}}{4\pi} i k_0 (2n+1) h_n(k_0 r_s^{\text{ex}}) j'_n(k_0 a_{\text{shell}}) + \frac{Q^{\text{shell}}}{4\pi} i k_1 (2n+1) h'_n(k_1 a_{\text{shell}}) j_n(k_1 r_s^{\text{shell}}) \end{aligned} \quad (\text{A12c})$$

$$\begin{aligned} & D_n j'_n(k_1 a_{\text{core}}) + E_n y'_n(k_1 a_{\text{core}}) - F_n j'_n(k_2 a_{\text{core}}) \\ &= -\frac{Q^{\text{shell}}}{4\pi} i k_1 (2n+1) h_n(k_1 r_s^{\text{shell}}) j'_n(k_1 a_{\text{core}}) + \frac{Q^{\text{core}}}{4\pi} i k_2 (2n+1) h'_n(k_2 a_{\text{core}}) j_n(k_2 r_s^{\text{core}}). \end{aligned} \quad (\text{A12d})$$

when $n = 0, 1, \dots, N$. Using the expressions in Eq. (A6) and the recurrence relations in Eq. (A5), we can solve Eq. (A12) to get coefficients C_n , D_n , E_n , F_n , and we then are able

to obtain the acoustic potential field driven by the acoustic monopoles located along the symmetric axis of a concentric core-shell spherical scatterer using the expressions in Eqs. (A8) to (A10).

Bohren, C., and Huffman, D. R. (1998). *Appendix A: Homogeneous Sphere*, 477–482 (John Wiley & Sons, Ltd),

<https://onlinelibrary.wiley.com/doi/abs/10.1002/9783527618156.app2>, doi: <https://doi.org/10.1002/9783527618156.app2>.

Burke, P. G., and Joachain, C. J. (1995). *Theory of Electron–Atom Collisions* (Springer US), <https://doi.org/10.1007/978-1-4899-1567-2>.

Burton, A. J., and Miller, G. F. (1971). “The application of integral equations to the numerical solution of some exterior boundary-value problems,” Proc. R. Soc. London, Ser. A **323**, 201 – 210.

Chernokozhin, E., Tsinovoy, A., and Amir, A. (2021). “Scattering by thin shells in fluids: Fast solver and experimental validation,” JASA Express Letters **1**, 016002.

DLMF (2020). “*NIST Digital Library of Mathematical Functions*” Release 1.1.0 of 2020-12-15, <http://dlmf.nist.gov/>, F. W. J. Olver, A. B. Olde Daalhuis, D. W. Lozier, B. I. Schneider, R. F. Boisvert, C. W. Clark, B. R. Miller, B. V. Saunders, H. S. Cohl, and M. A. McClain, eds.

Dümen, A. S., and Şaher, K. (2020). “Noise annoyance during COVID-19 lockdown: A research of public opinion before and during the pandemic,” The Journal of the Acousti-

cal Society of America **148**(6), 3489–3496, <https://doi.org/10.1121/10.0002667>, doi: [10.1121/10.0002667](https://doi.org/10.1121/10.0002667).

Emmanuelli, A., Dragna, D., Ollivier, S., and Blanc-Benon, P. (2021). “Characterization of topographic effects on sonic boom reflection by resolution of the euler equations,” The Journal of the Acoustical Society of America **149**(4), 2437–2450, <https://doi.org/10.1121/10.0003816>, doi: [10.1121/10.0003816](https://doi.org/10.1121/10.0003816).

Finneran, J. J. (2015). “Noise-induced hearing loss in marine mammals: A review of temporary threshold shift studies from 1996 to 2015,” The Journal of the Acoustical Society of America **138**(3), 1702–1726, <https://doi.org/10.1121/1.4927418>, doi: [10.1121/1.4927418](https://doi.org/10.1121/1.4927418).

Gonzalez, S., Salvi, D., Antonacci, F., and Sarti, A. (2021). “Eigenfrequency optimisation of free violin plates,” The Journal of the Acoustical Society of America **149**(3), 1400–1410, <https://doi.org/10.1121/10.0003599>, doi: [10.1121/10.0003599](https://doi.org/10.1121/10.0003599).

Hawkins, A. D., and Popper, A. N. (2018). “Directional hearing and sound source localization by fishes,” The Journal of the Acoustical Society of America **144**(6), 3329–3350, <https://doi.org/10.1121/1.5082306>, doi: [10.1121/1.5082306](https://doi.org/10.1121/1.5082306).

Hawkins, A. D., and Popper, A. N. (2020). “Sound detection by atlantic cod: An overview,” The Journal of the Acoustical Society of America **148**(5), 3027–3041, <https://doi.org/10.1121/10.0002363>, doi: [10.1121/10.0002363](https://doi.org/10.1121/10.0002363).

Helmholtz, H. (1896). *Theorie der Luftschwingungen in Röhren mit offenen Enden* (Verlag von Wilhelm Engelmann).

Kalayeh, K. M., Graf, J. S., and Gobbert, M. K. (2015). “FEM convergence for PDEs with point sources in 2-D and 3-D,” in *COMSOL Conference 2015*, Boston, MA, The United States, pp. 1–6.

Kinsler, L. E., Frey, A. R., Coppens, A. B., and Sanders, J. V. (2000). *Fundamentals of Acoustics*, 4th ed. (John Wiley and Sons Inc.).

Kirkup, S. (2007). *The Boundary Element Method in Acoustics*.

Klaseboer, E., Charlet, F. E. E., Khoo, B., Sun, Q., and Chan, D. Y. C. (2019). “Eliminating the fictitious frequency problem in BEM solutions of the external Helmholtz equation,” *Engineering Analysis with Boundary Elements* **109**, 106 – 116.

Klaseboer, E., Sun, Q., and Chan, D. Y. C. (2012). “Non-singular boundary integral methods for fluid mechanics applications,” *J. Fluid Mech.* **696**, 468–478.

Klaseboer, E., Sun, Q., and Chan, D. Y. C. (2017). “Nonsingular field-only surface integral equations for electromagnetic scattering,” *IEEE Transactions on Antennas and Propagation* **65**(2), 972–977.

Legg, M., and Bradley, S. (2016). “Measurement of stiffness of standing trees and felled logs using acoustics: A review,” *The Journal of the Acoustical Society of America* **139**(2), 588–604, <https://doi.org/10.1121/1.4940210>, doi: [10.1121/1.4940210](https://doi.org/10.1121/1.4940210).

Lugten, M., Karacaoglu, M., White, K., Kang, J., and Steemers, K. (2018). “Improving the soundscape quality of urban areas exposed to aircraft noise by adding moving water and vegetation,” *The Journal of the Acoustical Society of America* **144**, 2906.

Michaud, D. S., Fidell, S., Pearsons, K., Campbell, K. C., and Keith, S. E. (2007). “Review of field studies of aircraft noise-induced sleep disturbance,” *The Journal of the*

Acoustical Society of America **121**(1), 32–41, <https://doi.org/10.1121/1.2400613>, doi: [10.1121/1.2400613](https://doi.org/10.1121/1.2400613).

Mores, R. (2021). “Sound tuning in asymmetrically braced guitars,” The Journal of the Acoustical Society of America **149**(2), 1041–1057, <https://doi.org/10.1121/10.0003378>, doi: [10.1121/10.0003378](https://doi.org/10.1121/10.0003378).

Rivet, D., de Cacqueray, B., Sladen, A., Roques, A., and Calbris, G. (2021). “Preliminary assessment of ship detection and trajectory evaluation using distributed acoustic sensing on an optical fiber telecom cable,” The Journal of the Acoustical Society of America **149**(4), 2615–2627, <https://doi.org/10.1121/10.0004129>, doi: [10.1121/10.0004129](https://doi.org/10.1121/10.0004129).

Savioja, L., and Svensson, U. P. (2015). “Overview of geometrical room acoustic modeling techniques,” The Journal of the Acoustical Society of America **138**(2), 708–730, <https://doi.org/10.1121/1.4926438>, doi: [10.1121/1.4926438](https://doi.org/10.1121/1.4926438).

Sheng, X., Cheng, G., and Thompson, D. (2020). “Modelling wheel/rail rolling noise for a high-speed train running along an infinitely long periodic slab track,” The Journal of the Acoustical Society of America **148**, 174.

Stöber, U., and Thomsen, F. (2021). “How could operational underwater sound from future offshore wind turbines impact marine life?,” The Journal of the Acoustical Society of America **149**(3), 1791–1795, <https://doi.org/10.1121/10.0003760>, doi: [10.1121/10.0003760](https://doi.org/10.1121/10.0003760).

Sun, Q., Klaseboer, E., and Chan, D. Y. C. (2016). “A robust and accurate formulation of molecular and colloidal electrostatics,” The Journal of Chemical Physics **145**(5), 054106, <https://doi.org/10.1063/1.4960033>, doi: [10.1063/1.4960033](https://doi.org/10.1063/1.4960033).

Sun, Q., Klaseboer, E., and Chan, D. Y. C. (2017). “Robust multiscale field-only formulation of electromagnetic scattering,” *Phys. Rev. B* **95**(4), 045137, doi: [10.1103/PhysRevB.95.045137](https://doi.org/10.1103/PhysRevB.95.045137).

Sun, Q., Klaseboer, E., Khoo, B. C., and Chan, D. Y. (2014). “A robust and non-singular formulation of the boundary integral method for the potential problem,” *Engineering Analysis with Boundary Elements* **43**, 117–123, <https://doi.org/10.1016/j.enganabound.2014.03.010>, doi: [10.1016/j.enganabound.2014.03.010](https://doi.org/10.1016/j.enganabound.2014.03.010).

Sun, Q., Klaseboer, E., Khoo, B. C., and Chan, D. Y. C. (2013). “Stokesian dynamics of pill-shaped janus particles with stick and slip boundary conditions,” *Physical Review E* **87**(4), <https://doi.org/10.1103/physreve.87.043009>, doi: [10.1103/physreve.87.043009](https://doi.org/10.1103/physreve.87.043009).

Sun, Q., Klaseboer, E., Khoo, B. C., and Chan, D. Y. C. (2015a). “Boundary regularized integral equation formulation of Stokes flow,” *Physics of Fluids* **27**(2), 023102, <https://doi.org/10.1063/1.4907279>, doi: [10.1063/1.4907279](https://doi.org/10.1063/1.4907279).

Sun, Q., Klaseboer, E., Khoo, B.-C., and Chan, D. Y. C. (2015b). “Boundary regularized integral equation formulation of the Helmholtz equation in acoustics,” *R. Soc. Open Sci.* **2**(1), 140520.

Sun, Q., Klaseboer, E., Yuffa, A. J., and Chan, D. Y. C. (2020a). “Field-only surface integral equations: scattering from a dielectric body,” *Journal of the Optical Society of America A* **37**(2), 284, doi: [10.1364/josaa.37.000284](https://doi.org/10.1364/josaa.37.000284).

Sun, Q., Klaseboer, E., Yuffa, A. J., and Chan, D. Y. C. (2020b). “Field-only surface integral equations: scattering from a perfect electric conductor,” *Journal of the Optical*

Society of America A **37**(2), 276, doi: [10.1364/josaa.378665](https://doi.org/10.1364/josaa.378665).

Vorländer, M. (2013). “Computer simulations in room acoustics: Concepts and uncertainties,” The Journal of the Acoustical Society of America **133**(3), 1203–1213, <https://doi.org/10.1121/1.4788978>, doi: [10.1121/1.4788978](https://doi.org/10.1121/1.4788978).

Zhang, Z. (2016). “Mechanics of human voice production and control,” The Journal of the Acoustical Society of America **140**(4), 2614–2635, <https://doi.org/10.1121/1.4964509>, doi: [10.1121/1.4964509](https://doi.org/10.1121/1.4964509).